A Shared Control Architecture for Vitreoretinal Surgery with Safety Guarantee using Control Barrier Functions

Nicola Piccinelli[1], Federico Vesentini[1], Marius Briel[2], Ludwig Haide[2], Eleonora Tagliabue[2], Marco Pellegrini[3], Gernot Kronreif[4], and Riccardo Muradore[1]

***Abstract*—Control Barrier Functions (CBFs) provide a powerful framework for enforcing real-time safety in control systems and have seen increasing applications in safety-critical domains, such as surgical robotics. In vitreoretinal microsurgery, where precision and tissue protection are crucial, we propose a shared control approach that leverages CBFs to maintain the robot's end-effector within a safe zone above the retina. Using real-time 3D reconstruction from an instrument-integrated Optical Coherence Tomography (iiOCT) system mounted on the surgical tool, we define a safety band between two offset surfaces derived from the reconstructed retina. A hybrid controller drives the tool into the band when outside and then enforces forward invariance using a CBF-based quadratic program. Concurrently, haptic feedback proportional to the deviation from the band centre guides the surgeon toward the optimal working distance. We validate our method in ex vivo pig eye experiments, performing a simulated Vitreous Shaving (VS), showing improved safety and operator awareness.**

***Index Terms*—Shared Control, Control Barrier Function, Motion Planning, Collision Avoidance, Ophthalmic Surgery**

I. INTRODUCTION

Vitreoretinal surgery encompasses a range of delicate, micron-scale procedures designed to restore, preserve, or enhance vision in patients with retinal disorders. These interventions are performed within the confined interior of the eye using specialised microsurgical instruments such as cannulas, forceps, and endolaser probes, where precision is of paramount importance. The safety and effectiveness of these procedures critically depend on the surgeon's ability to perceive depth and perform fine manipulations. Depth perception is primarily derived from the microscope view, where surgeons must estimate sub-millimetric distances by visually comparing the instrument tip to its projected shadow, all while compensating for natural hand tremors [1].

Surgical robotic platforms offer promising solutions to the challenges inherent in vitreoretinal surgery by integrating advanced optical sensing technologies, as previously proposed [2]. These systems provide several key benefits, including motion scaling, tremor suppression, and accurate distance measurement, thereby enhancing surgical precision and safety.

In this paper, we present a shared control framework for vitreoretinal surgery that enables safe and precise navigation of tools relative to the retina. The approach combines intraoperative surface reconstruction via an instrument-integrated Optical Coherence Tomography (iiOCT), Control Barrier Functions (CBFs) for real-time safety enforcement, and haptic feedback for surgeon guidance. The retina is reconstructed as a smooth parametric surface $\mathcal{S}$ using iiOCT measurements, with two offset surfaces $\mathcal{S}_t$ and $\mathcal{S}_b$ defining a safety band around a desired working distance. A hybrid auto-depth controller drives the tool toward the band centre when outside and maintains it within bounds using a CBF-QP controller. Haptic feedback renders a force proportional to the deviation from the band centre, helping the operator maintain optimal depth. The method is validated on ex vivo pig eyes, showing improved safety and depth control during Vitreous Shaving (VS).

The main contributions of the paper are:

- a CBF-based control architecture to provide a safety distance from the retina surface,
- an ex vivo pig eye evaluation of the shared control architecture.

The paper is organised as follows. In Section II, we introduce the related work. In Section III, we describe the approach that we propose for the collision-free navigation of the surgical instrument above the retinal surface. In Section IV, the experimental setup and the obtained results are presented and discussed. Finally, in Section V we draw some conclusions and future work.

II. RELATED WORKS

Robotic systems for ophthalmic surgery have progressively evolved from handheld devices to fully teleoperated platforms, offering enhanced dexterity, precision, and motion scaling in submillimeter workspaces [3]. Early handheld systems, such as Micron [4], utilised piezoelectric actuators for active tremor cancellation, resulting in a 15 dB reduction in tool-tip vibration. Cooperative systems, such as the Steady-Hand Robot (SHER) [5], introduced admittance control and micro-force sensing to suppress tremor during delicate tasks, such as membrane peeling. In contrast, hybrid architectures, such as RAMIS [6], have improved stability through parallel–serial designs. However, these approaches primarily addressed motion precision and tremor suppression, rather than guaranteeing safe tool–tissue interaction in real-time. Teleoperated systems expanded these capabilities by decoupling the surgeon's hand motion from tool execution.

Platforms such as Preceyes Surgical System (PSS) [7] and IRISS [8] offered joystick-based control, motion scaling, and intraoperative OCT integration for subretinal injections and

---

This project has received funding from the European Union's Horizon Europe innovation actions under grant agreement No. 101070443 (GEYEDANCE).

[1] Department of Engineering for Innovation Medicine, University of Verona, Italy, [2] Carl Zeiss AG, Oberkochen, Germany, [3] Department of Translational Medicine, University of Ferrara, Italy, [4] ACMIT Gmbh, Wiener Neustadt, Austria

vein cannulation. Shared-control schemes emerged to blend human intent with autonomous safety constraints, relying on real-time sensing to assist the operator without removing control authority. Nonetheless, most of these frameworks implement heuristic safety limits rather than formal control constraints, leaving safety verification unaddressed. Haptic feedback has played a central role in improving user awareness and precision. In [9], a bilateral teleoperation system generated force feedback from manipulator positions only, without considering tissue proximity. Later works such as [10] leveraged OCT-based axial distance estimation to render pre-contact forces, and simulations in [11] demonstrated reduced surgical duration and tissue damage through haptic guidance. These approaches improved ergonomics but did not integrate force cues within a unified safety-control framework.

Optical Coherence Tomography (OCT) integration has been crucial for enabling shared autonomy. Fibre-based iiOCT systems [12] enabled real-time distance control using flat phantoms, while more recent works [13] introduced deep learning and dual-rate controllers for axial stabilisation. However, these methods often suffer from limited update rates or task-specific tuning. Vision-based approaches [14], [15] have been explored for planar control, but their performance is limited by calibration complexity and optical distortions. In contrast, iiOCT offers accurate, distortion-free depth sensing directly at the tool tip, which our framework exploits for local surface reconstruction and real-time safety monitoring. Recent iiOCT-based methods demonstrated motion tracking [16], surface reconstruction [17], and 6-DOF pose estimation [18]. While these sensing pipelines are essential, they have not been coupled with control-theoretic mechanisms ensuring safe operation. Similarly, adaptive and optimal control approaches [19] and virtual fixtures [20], [21] provide task assistance but rely on predefined boundaries rather than real-time reconstructed tissue models. Reinforcement learning has been applied to generate optimal trajectories [22], but it lacks interpretability and formal safety guarantees.

Our approach bridges these gaps by integrating iiOCT-based local surface reconstruction with CBFs framework, enforcing provable safety constraints during teleoperation, while providing continuous haptic feedback to the operator. In summary, prior works have advanced precision robotics, teleoperation, haptic rendering, and OCT sensing for vitreoretinal surgery, yet none provide formal, real-time safety assurance based on intraoperative sensory feedback. The proposed method uniquely combines iiOCT-driven environment reconstruction, model-based safety enforcement through CBFs, and haptic feedback within a shared-control architecture, ensuring both safety and the surgeon's situation awareness during microsurgical manipulation.

III. METHODOLOGY

We aim to provide a shared control architecture helping surgeons to keep a fixed distance d to the retina surface while performing critical tasks like VS. The methodology we are proposing is a hybrid controller composed of an initial attractor and a CBF-based optimal controller aiming to guarantee safety, i.e., keeping the end-effector within a safe band centred around d, i.e. $d \pm \delta$. The controllers are meant to: (i) be an *attractor* that drives the end-effector into the safe band if it starts outside, (ii) a *CBF-based optimal controller* that enforces forward invariance of the safe band once inside.

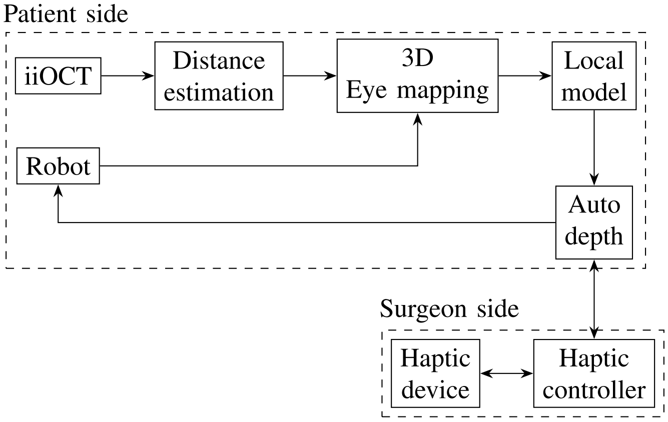

Fig. 1. Control architecture of the proposed shared control system.

The proposed system also provides force feedback to the operator via a haptic device to inform the surgeon if he/she is commanding the correct retinal distance. The control architecture, shown in Figure 1, is based on a priori local reconstruction of the retina surface. Such a reconstruction is obtained via an iiOCT mounted on the robot's end-effector, similar to [21]. In an iiOCT setup, a fibre-based probe embedded within the surgical instrument scans the tissue beneath the tool tip, providing the so-called A-scans, during manipulation. OCT is a non-invasive imaging technique that measures the echo time delay and intensity of backscattered light through low-coherence interferometry and reconstructs high-resolution cross-sectional images of biological tissue.

A. Local Retina Modelling and Safe Band Generation

The CBF-based controller requires a precise definition of the safe working area. We define this as a safe band bounded by two offset surfaces, $\mathcal{S}_t$ and $\mathcal{S}_b$, which represent the upper and lower boundaries of the acceptable working distance, $d \pm \delta$, from the retina. To generate this safe band, we must first obtain an accurate, smooth, and continuous geometric model $\mathcal{S}$ of the underlying retinal surface itself.

To achieve this, we employ the patient-specific geometrical modelling technique introduced in [23], which reconstructs the retina intraoperatively by integrating iiOCT measurements with robotic tracking. This method utilises Radial Basis Function (RBF) interpolation, which is chosen for its robustness to non-uniformly distributed point clouds acquired during surgery. It effectively balances noise suppression and surface fidelity through an optimised smoothing parameter, allowing for an accurate reconstruction of the retinal topology without imposing rigid global shape constraints (like spheres or ellipsoids). This process inherently accounts for uncertainties from 1D OCT A-scans and RCM-induced tracking inaccuracies [24].

Given a set of measured 3D points $\{\boldsymbol{p}_i = (x_i, y_i, z_i)\}_{i=1}^{n}$, the RBF technique finds an interpolation function $\hat{z}(x, y)$. The lateral 2D coordinates $\bar{\boldsymbol{p}}_i = (x_i, y_i)$ in the robot base frame (where the z-axis is angled at 30° from the world's upward direction) are used to construct the model

$$\hat{z}(\bar{p}) = \sum_{i=1}^{n} \alpha_i \phi(\|\bar{\boldsymbol{p}} - \bar{\boldsymbol{p}}_i\|) + \sum_{j=0}^{m} \beta_j \Pi_j(\bar{\boldsymbol{p}}), \tag{1}$$

where $\hat{z}(\bar{\boldsymbol{p}})$ is the local z-value approximation for a 2D point $\bar{\boldsymbol{p}}$, α_i, β_j are the interpolant coefficients, ϕ is a radially symmetric basis function, and Π_j are polynomials. The resulting function $s(\bar{\boldsymbol{p}})$ provides the continuous and physiologically consistent retinal model $\mathcal{S}$ that is well-suited for intraoperative use.

From this continuous model $\mathcal{S}$, we then generate the safe band. This is a multi-step process. First, we sample a dense point cloud $\{\boldsymbol{p}_i\}$ from the model $\mathcal{S}$. For each point $\boldsymbol{p}_i$, we estimate its local surface normal $\boldsymbol{n}_i$ by applying *Principal Component Analysis* (PCA) to its local neighbourhood. Since PCA does not guarantee a consistent orientation, a *Minimum Spanning Tree* (MST) propagation method is used to ensure all normals are oriented consistently [25]. Finally, the two boundary point clouds, $\mathcal{S}_t$ and $\mathcal{S}_b$, that define the safe band are generated by offsetting each point $\boldsymbol{p}_i$ along its unit normal $\boldsymbol{n}_i$

$$\mathcal{S}_t = \{\boldsymbol{p}_{i,t} \in \mathbb{R}^3 \,|\, \boldsymbol{p}_{i,t} = \boldsymbol{p}_i + (d + \delta)\boldsymbol{n}_i\},$$
$$\mathcal{S}_b = \{\boldsymbol{p}_{i,b} \in \mathbb{R}^3 \,|\, \boldsymbol{p}_{i,b} = \boldsymbol{p}_i + (d - \delta)\boldsymbol{n}_i\},$$

where d is the desired nominal safety distance from the retina and δ defines the half-thickness of the safe band, creating a total working thickness of 2δ centred at distance d.

When offsetting a point cloud along estimated normals to generate surfaces above and below the original geometry, self-intersections can occur, particularly in regions of high curvature or concavity. To mitigate this, an effective strategy is to first fit an implicit surface to the original point cloud, by using techniques such as Poisson surface reconstruction or RBFs and then extract offset surfaces as level sets

$$f(x) = d \pm \delta.$$

This method, introduced in [26], avoids fold-overs by ensuring that the offset surfaces are smooth and globally defined. Alternatively, one can adapt the offset distance based on the local curvature, reducing it in areas where large offsets would cause self-intersections. This involves estimating curvature via PCA eigenvalues or local surface fitting, and using an adaptive offset rule such as

$$d(\boldsymbol{p}_i) = \min(d_0, 1/\kappa(\boldsymbol{p}_i)),$$

where $\kappa(\boldsymbol{p}_i)$ is the curvature at point $\boldsymbol{p}_i$.

B. Shared Control with CBF Auto Depth

Let $\boldsymbol{x}(t) \in \mathbb{R}^3$ be the end-effector position in the robot base frame and let $\boldsymbol{v}^d(t) \in \mathbb{R}^3$ be its command linear velocity. The kinematic model of the end-effector can be represented as a single-integrator system in state-space form.

$$\dot{\boldsymbol{x}}(t) = \boldsymbol{v}^d(t). \tag{2}$$

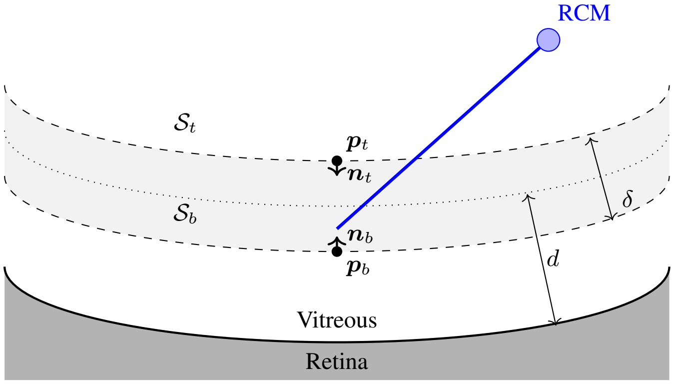

Fig. 2. Visualisation of the safe band relative to the retina surface. The dashed arcs represent the lower and upper boundary surfaces $\mathcal{S}_b$ and $\mathcal{S}_t$, defining a safe band of thickness δ. The tool (blue segment) extends through this band. Points $\boldsymbol{p}_b$ and $\boldsymbol{p}_t$ are the closest points on $\mathcal{S}_b$ and $\mathcal{S}_t$ with normals $\boldsymbol{n}_b$ and $\boldsymbol{n}_t$ directed inward. The distance d indicates the optimal distance from the retina (For illustration, the boundaries are vertically shifted approximations rather than exact normal offsets).

From the local point-cloud reconstruction of the retina, at each control cycle, we extract two shifted approximating surfaces (above and below the safe band). As shown in Figure 2, for the lower boundary surface $\mathcal{S}_b$, let $\boldsymbol{p}_b \in \mathbb{R}^3$ and $\boldsymbol{n}_b \in \mathbb{R}^3$ be the nearest point and the associated unit normal oriented so that $\boldsymbol{n}_b$ points into the safe band. Similarly, for the upper boundary surface $\mathcal{S}_t$, let $\boldsymbol{p}_t \in \mathbb{R}^3$ and $\boldsymbol{n}_t \in \mathbb{R}^3$ be the nearest point and the unit normal, respectively.

From each of the two surfaces, let $h_i(\boldsymbol{x})$, with $i \in \{b, t\}$, define the signed distance function as

$$h_i(\boldsymbol{x}) \;=\; \boldsymbol{n}_i^T(\boldsymbol{x} - \boldsymbol{p}_i) \tag{3}$$

such that $h_i(\boldsymbol{x}) \geq 0$ implies that $\boldsymbol{x}$ lies inside (or on) the boundary constraint, i.e., within the safe band. Due to (2), for each i, we have

$$\dot{h}_i(\boldsymbol{x}) = \nabla h_i(\boldsymbol{x})^T \dot{\boldsymbol{x}}(t) = \boldsymbol{n}_i^T \boldsymbol{v}^d(t). \tag{4}$$

The safe set can be defined as

$$\mathcal{C} = \mathcal{C}_b \cap \mathcal{C}_t, \tag{5}$$

where

$$\mathcal{C}_i = \left\{ \boldsymbol{x} \in \mathbb{R}^3 \mid h_i(\boldsymbol{x}) \geq 0 \right\} \quad i \in \{b, t\} \tag{6}$$

Given the safety definition (6), we aim to choose $\boldsymbol{v}^d(t)$ as close as possible to a reference linear velocity $\boldsymbol{v}^r(t)$ by solving a minimum norm Quadratic Programming (QP) optimisation problem. In case the end-effector is initially outside, first apply an attractor velocity $\boldsymbol{v}^a(t)$ that drives $\boldsymbol{x}(t)$ into the safe set $\mathcal{C}$.

To design an attractor velocity $\boldsymbol{v}^a(t)$ steering $\boldsymbol{x}(t)$ into $\mathcal{C}$, we first define the signed distance to the band centre and the average normal as

$$d_c(\boldsymbol{x}) = \frac{1}{2}\big(h_t(\boldsymbol{x}) - h_b(\boldsymbol{x})\big), \quad \boldsymbol{n}_c = \frac{1}{2}(\boldsymbol{n}_t - \boldsymbol{n}_b); \tag{7}$$

then, the attractor velocity is given by a spring-like feedback

$$\boldsymbol{v}^a = -k_{\text{att}} d_c(\boldsymbol{x}) \boldsymbol{n}_c, \tag{8}$$

where $k_{\text{att}} > 0$ is an application-dependent parameter. A candidate Lyapunov function is

$$V(\boldsymbol{x}) = \tfrac{1}{2} d_c(\boldsymbol{x})^2, \tag{9}$$

with

$$\dot{V}(\boldsymbol{x}) = d_c(\boldsymbol{x}) \boldsymbol{n}_c^T \boldsymbol{v}^a(t). \tag{10}$$

Substituting (8) in (10) yields

$$\dot{V}(\boldsymbol{x}) = -k_{\text{att}}\, d_c(\boldsymbol{x})^2 \, \|\boldsymbol{n}_c\|^2 < 0, \quad \text{for } d_c(\boldsymbol{x}) \neq 0, \tag{11}$$

which guarantees that $\boldsymbol{x}(t)$ converges to the band center. Once inside the safe band, the attractor is turned off, and the command velocity is determined by solving the QP problem. We consider the straight line $\gamma h_i(\boldsymbol{x})$, with $\gamma > 0$, as a class-$\mathcal{K}$ function. The CBF [27] conditions require

$$\dot{h}_i(\boldsymbol{x}) + \gamma\, h_i(\boldsymbol{x}) \geq 0 \iff \boldsymbol{n}_i^T \boldsymbol{v}^d + \gamma\, h_i(\boldsymbol{x}) \geq 0. \tag{12}$$

for every i. When $h_i(\boldsymbol{x}) = 0$ (on boundary), this reduces to $\boldsymbol{n}_i^T \boldsymbol{v} \geq 0$, preventing exit. If $h_i(\boldsymbol{x}) > 0$, the inequality admits a range of $\boldsymbol{v}$. Thus, the feasible set $\{\boldsymbol{v}^d \mid \boldsymbol{n}_i^T \boldsymbol{v}^d + \gamma h_i(\boldsymbol{x}) \geq 0,\ i = b, t\}$ is nonempty whenever $h_i(\boldsymbol{x}) \geq 0$.

To find the closest $\boldsymbol{v}^d$ to the reference velocity $\boldsymbol{v}^r$ subject to the barrier constraints, we solve the following constrained QP

$$\begin{aligned} \boldsymbol{v}^* = \underset{\boldsymbol{v}^d \in \mathbb{R}^3}{\arg\min}\ & \tfrac{1}{2} \|\boldsymbol{v}^d(t) - \boldsymbol{v}^r(t)\|_2^2 \\ \text{s.t.}\ \boldsymbol{n}_b^T \boldsymbol{v}^d(t) + \gamma\, h_b(\boldsymbol{x}) \ &\geq\ 0, \\ \boldsymbol{n}_t^T \boldsymbol{v}^d(t) + \gamma\, h_t(\boldsymbol{x}) \ &\geq\ 0. \end{aligned} \tag{13}$$

This convex QP in $\mathbb{R}^3$ with two linear inequality constraints admits a unique global minimum $\boldsymbol{v}^*$. The unconstrained optimal solution is simply $\boldsymbol{v}^d = \boldsymbol{v}^r$. If $\boldsymbol{v}^r$ satisfies both CBF constraints, then it remains the optimal solution, i.e., $\boldsymbol{v}^* = \boldsymbol{v}^r$. Otherwise, the optimal solution $\boldsymbol{v}^*$ is the projection of $\boldsymbol{v}^r$ onto the feasible set defined by the two inequality constraints.

The shared control strategy combines the proposed auto-depth controller with an existing passivity-based bilateral force-velocity teleoperation framework [28]. In this architecture, the modulated velocity computed by the remote side is the nominal desired velocity $\boldsymbol{v}^r(t)$ for the auto-depth module. If the end-effector position $\boldsymbol{x}$ satisfies both barrier constraints, that is, $h_b(\boldsymbol{x}) > 0$ and $h_t(\boldsymbol{x}) > 0$, then the safety set $\mathcal{C}$ is maintained, and the robot directly executes the nominal velocity without further modification.

However, force feedback to the operator is not designed to be zero when inside the safe band, but specifically when the tool is precisely at the centre of the band, corresponding to the target retinal working distance. As the end-effector deviates from the band centre toward either boundary, a repulsive force proportional to this deviation is rendered to the user, guiding them back toward the centre of the optimal safe zone.

Formally, the force feedback is defined as

$$\boldsymbol{f}^h(t) = k_{\text{rep}}\, d_c(\boldsymbol{x})\, \boldsymbol{n}_c, \tag{14}$$

where $k_{\text{rep}} > 0$ is an application-dependent gain. This force points inward the band centre and increases linearly with the signed distance $d_c(\boldsymbol{x})$, thus intuitively informing the operator of both the direction and magnitude needed to maintain the ideal surgical distance. To ensure comfort and safety, the resulting force magnitude is clamped to a user-defined maximum $\|\boldsymbol{f}^h(t)\| \leq f_{\max}$. This haptic cue enhances situation awareness, effectively fusing robot autonomy and operator intent for safe and precise retinal manipulation.

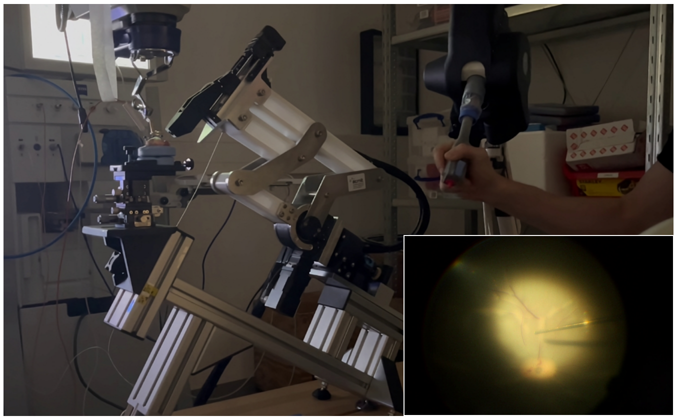

Fig. 3. Experimental setup used for the ex vivo evaluation. The system comprises a haptic device coupled with a patient-side manipulator developed by ACMIT Gmbh. A Zeiss microscope provides the visual feedback, while the OCT engine is also supplied by ACMIT Gmbh. The inset shows a microscope view of the porcine eye fundus with the robotic instrument visible on the right side.

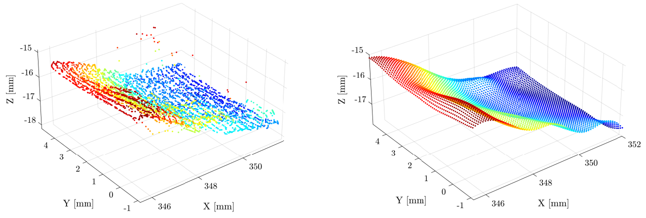

(a) Raw data

(b) Local model

Fig. 4. The raw data acquired using the iiOCT in comparison with the resulting surface using the local modelling reconstruction (the colour represents the depth in the z-axis of the robot's base frame). (a) the raw point cloud, (b) the local model sampled surface.

IV. Experimental results

The experimental setup is shown in Figure 3, and it is similar to [21]. The OCT engine and the patient-side manipulator named Gear (ACMIT Gmbh, Austria). The two manipulators have four degrees of freedom and are both interfaced using ROS. The vision system is a ZEISS Artevo 850 digital microscope (Zeiss AG, Germany). The Gear robot is equipped with an iiOCT probe used for intraoperative OCT scanning, featuring a scanning range of $12\,\text{mm}$. The range is limited by both the optical and mechanical constraints of the interferometer, as well as the physical pixel resolution required for reconstruction. We utilised a deep learning algorithm to estimate the tool-to-tissue distance [21].

The control frequency of the overall system is $50\,\text{Hz}$ while the bilateral teleoperation architecture operates at $100\,\text{Hz}$. Given the low-frequency nature of vitreoretinal manipulation and the passivity-based control scheme, this bandwidth is

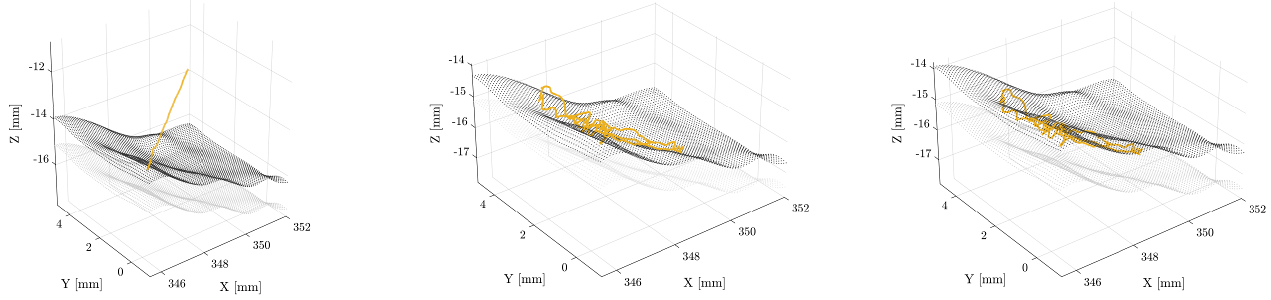

(a) Approaching path

(b) Vitrectomy bottom surface

(c) Vitrectomy top surface

Fig. 5. The robot's end-effector motion during the experiment (in yellow, the traced path of the end-effector over time). (a) The end-effector path during the approach to the safe set, (b) the end-effector path during the vitrectomy and the bottom surface of the safe set, (c) the end-effector path during the vitrectomy and the top surface of the safe set.

sufficient to ensure smooth and stable force feedback while preserving transparency in the teleoperation loop. The OCT engine and the computer running the robot's and the haptic device's driver were synchronised using the Network Time Protocol (NTP). The experiment is performed using an ex vivo porcine eye in a "closed sky" condition, as shown in Figure 3. The eye is mounted on a custom-made 3D-printed eye holder.

To prepare for the experiment, we first performed an automatic grid scan with a side length of $6\,\mathrm{mm}$ and a grid spacing of $50\,\mathrm{\mu m}$, requiring a scan time of $90\,\mathrm{s}$. The resulting raw point cloud, including visible outliers, is shown in Figure 4b. From this initial scan, we used RBF-based reconstruction [29] to obtain a smooth local model, which was then discretised using the same grid spacing. The final model of the porcine eye is shown in Figure 4. No further refinements were required to address fold-over effects during surface offsetting, as the initial surface regularity was sufficiently for the indentation distance required by the task.

A. Ex-vivo Vitreous Shaving

To evaluate the effectiveness of the proposed method, we performed a vitreous shaving near the retinal surface, maintaining a constant distance of $1\,\mathrm{mm}$ from the retinal surface with a symmetric safe band of $400\,\mathrm{\mu m}$. Thus, the distance of the bottom surface $\mathcal{S}_b$ is $800\,\mathrm{\mu m}$ and the distance of the top surface $\mathcal{S}_t$ is $1200\,\mathrm{\mu m}$. The desired velocity $\boldsymbol{v}^d(t)$ is the end-effector velocity of the haptic device mapped into the patient-side reference frame accordingly to the bilateral teleoperation platform proposed in [21]. We set the CBF parameter $\gamma = 10$ for both the top and bottom surfaces.

As shown in Figure 5a, the robot's tool tip is several millimetres above the safe band. In this phase, the attractor velocity $\boldsymbol{v}^a(t)$ is computed with a stiffness set to $k_{att} = 1$, and the controller slowly drives the end-effector towards the closest point on the top surface. During this initial approach phase, the patient-side manipulator is disconnected from the teleoperation system and is automatically driven towards the safe band. Figure 7c shows that the values of the two CBFs keep decreasing until, around $110\,\mathrm{s}$, the end-effector is within the band, and the shared control is activated.

TABLE I

TRACKING ERROR METRICS BETWEEN DESIRED AND MODULATED POSITIONS UNDER THE CBF-BASED CONTROLLER (VALUES IN mm).

	x-axis	y-axis	z-axis	Overall
RMSE	0.1508	0.1648	0.1048	0.1401
STD	0.1464	0.1640	0.1033	0.1379
MAE	0.1044	0.1241	0.0780	0.1022
MAXE	0.5538	0.5465	0.2978	0.4660

From $110\,\mathrm{s}$, the operator then controls the system, moving the robot above the retina to mimic the motion of the vitrectomy. As shown in Figure 5, the end-effector moves successfully between the top and bottom surface, with an overall tracking error Root Mean Square Error (RMSE) of $140\,\mathrm{\mu m}$ and with a Maximum Error (MAXE) of $460\,\mathrm{\mu m}$, see Table I for the error metrics along each axis. The maximum error happens when the operator tries to push the haptic device towards the safe set boundary, as shown in Figure 6. Nonetheless, since the teleoperation platform we are using is equipped with a clutch, the operator can recover from the misalignment whenever needed.

The force feedback perceived by the operator is shown in Figure 6 and is obtained using $k_{\text{rep}} = 20000$ and $f_{\max} = 5\,\mathrm{N}$. The gain k_{rep} was chosen to generate a smooth force gradient, equivalent to $2\,\mathrm{N}$ per $100\,\mu m$ of deviation from the safe-band centre. This tuning ensures that small displacements from the desired working distance provide clear haptic cues without exceeding the comfortable force range of the device. The maximum feedback force $f_{\max}$ was set higher than the force associated with the full safe-band width to prevent early saturation. The main interaction the user experienced while trying to maintain a constant distance occurred along the x and z directions of the robot's base reference frame. In general, the force feedback intervenes frequently until the robot is not kept within the safe band, where the desired eye depth is located.

Figure 7 shows the behaviour over time of the tool-to-tissue distance. It is worth noticing that the proposed control system is always able to effectively guarantee the feasibility of the optimisation problem. In fact, as shown in Figure 7c, once the end-effector enters the safety set, it never escapes it. Figure 7b

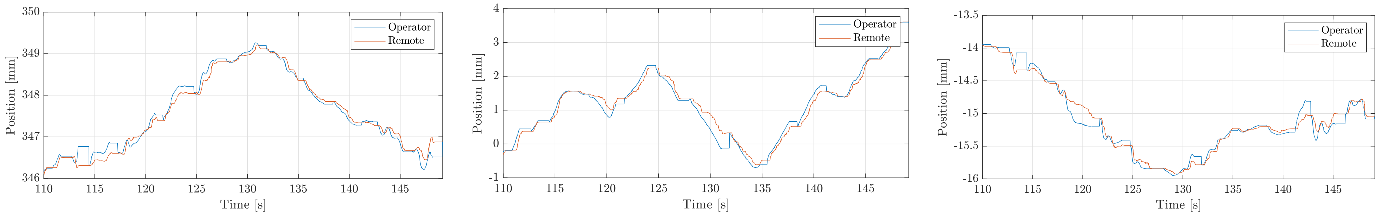

(a) x axis (b) y axis (c) z axis

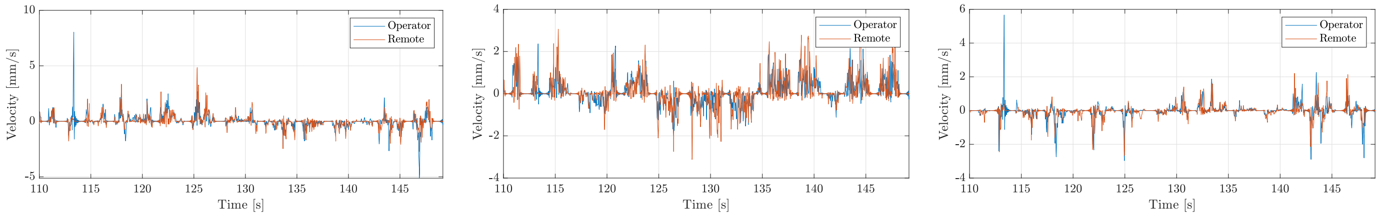

(d) x axis (e) y axis (f) z axis

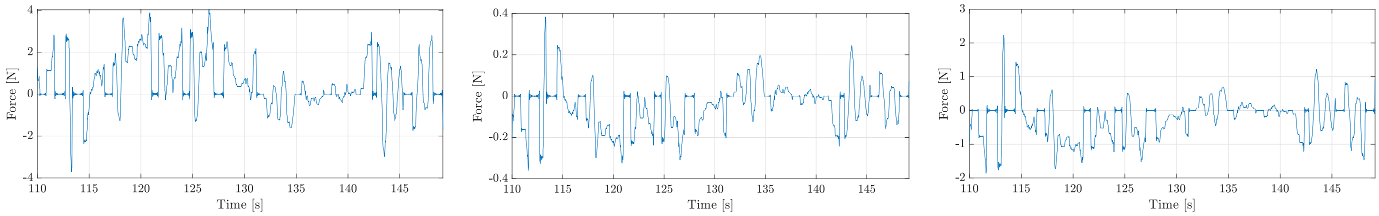

(g) x axis (h) y axis (i) z axis

Fig. 6. The operator and remote-side Cartesian positions, velocities, and force feedback during the shared control within the safe bounds. (a)-(c) Cartesian positions along the x, y, and z directions, (d)-(f) Cartesian velocities along the x, y, and z directions, (g)-(i) wrenches perceived by the operator along the x, y, and z directions.

shows the norm of the force feedback vector commanded to the haptic device. It is possible to see that, between $130\,\mathrm{s}$ and $140\,\mathrm{s}$, accordingly to (14), the force goes near zero when the operator is able to keep the patient-side robot at the right height. It increases to its maximum when the end-effector is at one of the two safe band boundaries (around $115\,\mathrm{s}$ and $125\,\mathrm{s}$).

Finally, in Figure 7a, the distance estimated using the iiOCT is compared with the axial distance estimated using the intersection point of the tool axis and the local model. This shows a coherent measurement of the closest point on the retina along the axial direction. However, for the task performed, using the raw distance provided by the sensor is insufficient to guarantee the desired tool-to-tissue distance. In fact, the sensor measures the distance only in the axial direction, while in this case, the safety condition is defined with respect to the closest point to the retina, which is clearly not in the axial direction. Another interesting motivation is due to the intrinsic error in the estimated distance, which also occurred in our experimental evaluation around $115\,\mathrm{s}$ and $120\,\mathrm{s}$. In these cases, the confidence of the distance estimator went well below the average value, resulting in very large outliers.

B. Clinical Applicability and Discussion

We further assessed the clinical relevance of the proposed framework through an experiment conducted with an experienced vitreoretinal surgeon. The performance of the proposed shared-control system was compared against two alternative configurations: (1) unilateral teleoperation VS, and (2) CBF-based safety enforcement at the remote side without haptic feedback. To ensure repeatability, the evaluation was performed on a synthetic eye phantom, and the surgeon was instructed to start each trial from a comparable initial position, interacting with the same retinal region.

In vitreoretinal surgery, maintaining a controlled and close distance to the retinal surface is of critical importance, particularly during vitreous shaving. Excessive or aggressive shaving can induce retinal tears, which may progress to retinal detachment if not promptly managed. The traction exerted on the retina during this manoeuvre can stress fragile areas or exacerbate pre-existing weaknesses. Furthermore, involuntary damage to retinal blood vessels can cause bleeding or intraoperative haemorrhage, complicating the procedure and recovery. Therefore, precise depth control and avoidance of excessive traction are essential to minimise these risks. A system that provides depth-guided manipulation can assist surgeons in achieving maximum vitreous removal while maintaining a safe buffer from the retina.

The RMSE of the tool-to-retina distance with respect to the desired working distance of $1\,\mathrm{mm}$ was $114\,\mu\mathrm{m}$ with haptic feedback, $115\,\mu\mathrm{m}$ without haptic feedback, and $250\,\mu\mathrm{m}$ during unilateral teleoperation. The end-effector total travel distances were $37.36\,\mathrm{mm}$, $21.40\,\mathrm{mm}$, and $44.59\,\mathrm{mm}$, respectively. The corresponding task durations were $83.29\,\mathrm{s}$, $46.29\,\mathrm{s}$, and $86.70\,\mathrm{s}$, resulting in comparable average execution speeds of $0.44\,\mathrm{mm\,s^{-1}}$, $0.46\,\mathrm{mm\,s^{-1}}$, and $0.51\,\mathrm{mm\,s^{-1}}$. The

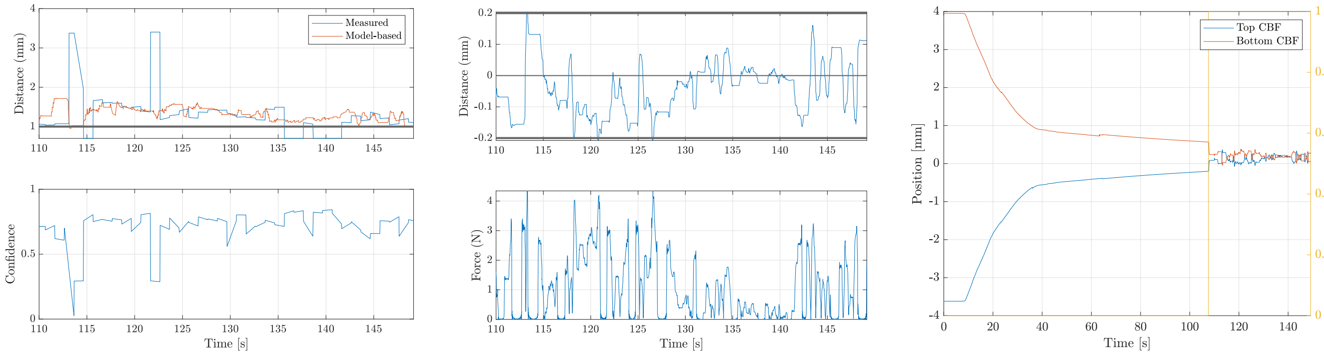

(a) Estimated tool-to-tissue distance (b) Safe band haptic feedback (c) CBF values over time

Fig. 7. The distance constraints evolution over time during the experimental validation. (a) Estimated tool-to-tissue distance using iiOCT (top) and the associated confidence level (bottom). (b) End-effector distance relative to the centre of the safe band and the magnitude of the haptic force feedback applied. (c) CBF values for the top (blue) and bottom (orange) surfaces during the experiment, with the yellow line indicating whether the end-effector is inside or outside the safe band.

results indicate that the addition of safety constraints does not substantially increase task duration, while providing more consistent control of the working distance.

According to the surgeon's feedback, the CBF-based safety constraint at the remote side significantly improved confidence during manipulation, by reducing perceived workload and the need for continuous visual estimation of depth. The haptic feedback was perceived as informative, but not essential, likely because strong visual cues were available and the forces typically encountered in retinal surgery are minimal. Nevertheless, the combination of real-time safety enforcement and haptic guidance enhanced overall situation awareness and could be particularly valuable in scenarios with limited visual feedback or when operating near delicate tissue structures. The experimental results also highlighted the limitations of relying solely on axial iiOCT distance measurements for safe tool control, motivating the use of model-based approaches as we proposed. Finally, the cases in which haptic feedback did not lead to performance improvements deserve further discussion. This behaviour may be related to limitations in the transparency of the rendered force feedback and potential inconsistencies between visual and haptic information. Moreover, given the high level of expertise of the surgeon involved, haptic cues may have been perceived as redundant, whereas their contribution could be more evident for less experienced users or in conditions with reduced visual feedback.

V. CONCLUSIONS

In this paper, we present a shared-control system for vitreoretinal surgery, designed to maintain a safe and precise tool-to-tissue distance during critical tasks. The approach integrates a CBF-based optimal controller with an initial attractor controller to enforce forward invariance within a predefined safe band. A patient-specific retinal model was constructed from intraoperative OCT scans using radial basis functions, allowing for smooth surface reconstruction and offset-based safety boundaries. Integrated into a bilateral teleoperation setup, the system allows intuitive operator control with automatic depth modulation and haptic feedback. Ex vivo tests on porcine eyes demonstrated that the controller reliably maintained tool safety. A preliminary evaluation by an experienced surgeon confirmed an improvement in confidence and a reduction in workload. Future work will extend in vivo validation, incorporate dynamic retinal deformation models, and conduct a cognitive workload analysis of surgeons.

REFERENCES

[1] C. N. Riviere, R. S. Rader, and P. K. Khosla, "Characteristics of hand motion of eye surgeons," in *Proceedings of the 19th Annual International Conference of the IEEE Engineering in Medicine and Biology Society*, 1997, pp. 1690–1693.

[2] E. Vander Poorten, C. N. Riviere, J. J. Abbott, C. Bergeles, M. A. Nasseri, J. U. Kang, R. Sznitman, K. Faridpooya, and I. Iordachita, "36 - Robotic retinal surgery," in *Handbook of Robotic and Image-Guided Surgery*, 2020, pp. 627–672.

[3] H. Mi, R. E. MacLaren, and J. Cehajic-Kapetanovic, "Robotising vitreoretinal surgeries," *Eye*, pp. 1–10, 2024.

[4] R. A. MacLachlan, B. C. Becker, J. C. Tabares, G. W. Podnar, L. A. Lobes, and C. N. Riviere, "Micron: an actively stabilized handheld tool for microsurgery," *IEEE transactions on robotics*, vol. 28, no. 1, pp. 195–212, 2011.

[5] A. Üneri, M. A. Balicki, J. Handa, P. Gehlbach, R. H. Taylor, and I. Iordachita, "New steady-hand eye robot with micro-force sensing for vitreoretinal surgery," in *2010 3rd IEEE RAS & EMBS International Conference on Biomedical Robotics and Biomechatronics*. IEEE, 2010, pp. 814–819.

[6] M. A. Nasseri, M. Eder, S. Nair, E. Dean, M. Maier, D. Zapp, C. P. Lohmann, and A. Knoll, "The introduction of a new robot for assistance in ophthalmic surgery," in *2013 35th Annual International Conference of the IEEE Engineering in Medicine and Biology Society (EMBC)*. IEEE, 2013, pp. 5682–5685.

[7] D. A. Maberley, M. Beelen, J. Smit, T. Meenink, G. Naus, C. Wagner, and M. D. de Smet, "A comparison of robotic and manual surgery for internal limiting membrane peeling," *Graefe's Archive for Clinical and Experimental Ophthalmology*, vol. 258, no. 4, pp. 773–778, 2020.

[8] J. T. Wilson, M. J. Gerber, S. W. Prince, C.-W. Chen, S. D. Schwartz, J.-P. Hubschman, and T.-C. Tsao, "Intraocular robotic interventional surgical system (iriss): Mechanical design, evaluation, and master–slave manipulation," *The International Journal of Medical Robotics and Computer Assisted Surgery*, vol. 14, no. 1, p. e1842, 2018.

[9] A. Barthel, D. Trematerra, M. A. Nasseri, D. Zapp, C. P. Lohmann, A. Knoll, and M. Maier, "Haptic interface for robot-assisted ophthalmic surgery," *37th Annual International Conference of the IEEE Engineering in Medicine and Biology Society*, pp. 4906–4909, 2015.

[10] R. Mieling, C. Stapper, S. Gerlach, M. Neidhardt, S. Latus, M. Gromniak, P. Breitfeld, and A. Schlaefer, "Proximity-based haptic feedback for collaborative robotic needle insertion," in *Haptics: Science, Technology, Applications*, 2022, vol. 13235, pp. 301–309.

[11] A. Francone, J. M. Huang, J. Ma, T.-C. Tsao, J. Rosen, and J.-P. Hubschman, "The effect of haptic feedback on efficiency and safety during preretinal membrane peeling simulation," *Translational Vision Science & Technology*, vol. 8, no. 4, 2019.

[12] M. Balicki, J.-H. Han, I. Iordachita, P. Gehlbach, J. Handa, R. Taylor, and J. Kang, "Single fiber optical coherence tomography microsurgical instruments for computer and robot-assisted retinal surgery," in *Medical Image Computing and Computer-Assisted Intervention – MICCAI*, 2009, pp. 108–115.

[13] S. Lee and J. Kang, "CNN-based CP-OCT sensor integrated with a subretinal injector for retinal boundary tracking and injection guidance," *Journal of Biomedical Optics*, vol. 26, no. 6, 2021.

[14] S. Yang, J. N. Martel, L. A. LobesJr, and C. N. Riviere, "Techniques for robot-aided intraocular surgery using monocular vision," *The International Journal of Robotics Research*, vol. 37, no. 8, pp. 931–952, 2018.

[15] R. Peter, S. Moreira, E. Tagliabue, M. Hillenbrand, R. G. Nunes, and F. Mathis-Ullrich, "Stereo reconstruction from microscopic images for computer-assisted ophthalmic surgery," *International Journal of Computer-Assisted Radiology and Surgery*, vol. 20, no. 3, pp. 605–612, 2025.

[16] P. Xu, M. Ourak, G. Borghesan, and E. Vander Poorten, "Fast oct based needle tracking for retinal microsurgery using dynamic spiral scanning," *IEEE Transactions on Medical Robotics and Bionics*, 2024.

[17] M. Sommersperger, J. Weiss, M. Ali Nasseri, P. Gehlbach, I. Iordachita, and N. Navab, "Real-time tool to layer distance estimation for robotic subretinal injection using intraoperative 4d oct," *Biomedical Optics Express*, vol. 12, no. 2, pp. 1085–1104, 2021.

[18] M. Zhou, X. Hao, A. Eslami, K. Huang, C. Cai, C. P. Lohmann, N. Navab, A. Knoll, and M. A. Nasseri, "6dof needle pose estimation for robot-assisted vitreoretinal surgery," *IEEE Access*, vol. 7, pp. 63 113–63 122, 2019.

[19] A. Ebrahimi, M. G. Urias, N. Patel, R. H. Taylor, P. Gehlbach, and I. Iordachita, "Adaptive control improves sclera force safety in robot-assisted eye surgery: A clinical study," *IEEE Transactions on Biomedical Engineering*, vol. 68, no. 11, pp. 3356–3365, 2021.

[20] B. C. Becker, R. A. MacLachlan, L. A. Lobes, G. D. Hager, and C. N. Riviere, "Vision-based control of a handheld surgical micromanipulator with virtual fixtures," *IEEE Transactions on Robotics*, vol. 29, no. 3, pp. 674–683, 2013.

[21] N. Piccinelli, L. Haide, M. Briel, A. Jungo, E. Tagliabue, T. D. Col, M. Schmid, R. Sznitman, M. Pellegrini, A. C. Yu, M. Busin, M. Mura, R. Muradore, and G. Kronreif, "Geyedance: An oct-enhanced multimodal feedback platform for robot-assisted ophthalmic surgery," *IEEE Transactions on Medical Robotics and Bionics*, pp. 1–1, 2025.

[22] J. W. Kim, P. Zhang, P. Gehlbach, I. Iordachita, and M. Kobilarov, "Towards autonomous eye surgery by combining deep imitation learning with optimal control," in *Conference on Robot Learning*. PMLR, 2021, pp. 2347–2358.

[23] M. Briel, L. Haide, J. Emmrich, N. Piccinelli, G. Kronreif, E. Tagliabue, and F. Mathis-Ullrich, "Intraoperative 3d reconstruction and geometric modeling using sensorized microsurgical instruments," *IEEE Transactions on Medical Robotics and Bionics*, 2025.

[24] M. Briel, L. Haide, M. Hess, J. Schimmelpfennig, P. Matten, R. Peter, M. Hillenbrand, E. Tagliabue, and F. Mathis-Ullrich, "Intraoperative adaptive eye model based on instrument-integrated oct for robot-assisted vitreoretinal surgery," *International Journal of Computer Assisted Radiology and Surgery*, vol. 20, no. 5, pp. 881–889, 2025.

[25] H. Hoppe, T. DeRose, T. Duchamp, J. McDonald, and W. Stuetzle, "Surface reconstruction from unorganized points," in *Proceedings of the 19th annual conference on computer graphics and interactive techniques*, 1992, pp. 71–78.

[26] M. Kazhdan, M. Bolitho, and H. Hoppe, "Poisson surface reconstruction," in *Proceedings of the fourth Eurographics symposium on Geometry processing*, vol. 7, no. 4, 2006.

[27] A. D. Ames, S. Coogan, M. Egerstedt, G. Notomista, K. Sreenath, and P. Tabuada, "Control barrier functions: Theory and applications," in *2019 18th European control conference (ECC)*. Ieee, 2019, pp. 3420–3431.

[28] N. Piccinelli, G. Colombo-Taccani, and R. Muradore, "A passive convex optimal control algorithm for teleoperating a redundant robotic arm in minimally invasive surgery," *International Journal of Robust and Nonlinear Control*, vol. 35, no. 10, pp. 4132–4148, 2025.

[29] U. Nguyen, L. Laaksonen, H. Uusitalo, and L. Lensu, "Reconstruction of retinal spectra from rgb data using a rbf network," in *2016 Sixth International Conference on Image Processing Theory, Tools and Applications (IPTA)*. IEEE, 2016, pp. 1–6.